On the choice of outlet boundary conditions for patient-specific analysis of aortic flow using computational fluid dynamics

S. Pirola[a], Z. Cheng[a], O. A. Jarral[b], D. P. O'Regan[c], J.R. Pepper[d], T. Athanasiou[b], X. Y. Xu[a,*]

[a]Department of Chemical Engineering, Imperial College London, South Kensington Campus, London SW7 2AZ, UK

[b]Department of Surgery and Cancer, St. Mary's Hospital, Imperial College London, UK

[c]MRC London Institute of Medical Sciences, , Hammersmith Hospital, Imperial College London, UK

[d]Royal Brompton and Harefield NHS Foundation Trust, Sydney Street, London SW3 6NP, UK

* Corresponding author. Tel.: +44 (0)2075945588; E-mail: yun.xu@imperial.ac.uk

ABSTRACT

Boundary conditions (BCs) are an essential part in computational fluid dynamics (CFD) simulations of blood flow in large arteries. Although several studies have investigated the influence of BCs on predicted flow patterns and hemodynamic wall parameters in various arterial models, there is a lack of comprehensive assessment of outlet BCs for patient-specific analysis of aortic flow. In this study, five different sets of outlet BCs were tested and compared using a subject-specific model of a normal aorta. Phase-contrast magnetic resonance imaging (PC-MRI) was performed on the same subject and velocity profiles extracted from the *in vivo* measurements were used as the inlet boundary condition. Computational results obtained with different outlet BCs were assessed in terms of their agreement with the PC-MRI velocity data and key hemodynamic parameters, such as pressure and flow waveforms and wall shear stress related indices. Our results showed that the best overall performance was achieved by using a well-tuned three-element Windkessel model at all model outlets, which not only gave a good agreement with *in vivo* flow data, but also produced physiological pressure waveforms and values. On the other hand, opening outlet BCs with zero pressure at multiple outlets failed to reproduce any physiologically relevant flow and pressure features.

Keywords: *Computational fluid dynamics (CFD), boundary conditions, Windkessel model, patient-specific simulation, hemodynamics, aorta*

Introduction

3D patient-specific computational models can provide valuable insights into hemodynamic and biomechanical conditions in the cardiovascular system. However, 3D modelling of the whole vascular tree is time-consuming and requires high computational costs. Therefore, computational simulations are commonly performed on specific regions of interest, e.g. the aorta or its segments. The excluded sections of the cardiovascular system must then be taken into account by exploiting model boundary conditions (BCs), which are a key part in the development of effective computational fluid dynamics (CFD) and fluid structure interaction (FSI) models. The importance of realistic BCs has already been highlighted in several studies (Morbiducci et al 2010; Morbiducci et al 2013; Gallo et al. 2012; Campbell et al., 2012), which showed that different BCs could lead to quantitative differences in the resulting flow rates, velocity fields and wall shear stress (WSS).

The choice of outlet BCs is of particular importance and different outlet BCs have been adopted in an attempt to better reproduce *in vivo* hemodynamic conditions in the cardiovascular system. Despite their recognised importance (Augst et al., 2003; Gallo et al., 2012; Morbiducci et al., 2010; Van der Giessen et al., 2011; Vignon-Clementel et al., 2006), only a few studies have compared the commonly used outlet BCs for aortic CFD models. Gallo et al. (2012) studied the influence of outflow BCs derived from phase-contrast magnetic resonance imaging (PC-MRI) data on predicted flow distributions and wall shear stress (WSS), demonstrating the importance of using patient-specific instantaneous flow rate distribution. However, this work did not include Windkessel-based outlet BCs which describe the pressure-flow relationship at each outlet.

Morbiducci and colleagues (2010) compared outflow and Windkessel BCs in a subject-specific model of the carotid bifurcation. By comparing CFD results obtained with three different fixed flow divisions and Windkessel model at the outlets, they showed that Windkessel-based outlet BC was able to reproduce realistic flow conditions. This is important in the development of effective BCs, especially because a complete set of patient-specific instantaneous flow data may not always be available. Different outlet BCs have been used in aortic models, mostly depending on the data availability, which always represents a challenge for patient-specific simulations. In the present study, we aim to quantify the influence of different types of outlet BCs on aortic hemodynamics assessment. For this purpose, a patient-specific model of a healthy human aorta was employed together with five sets of the most commonly used outlet BCs, including Windkessel model, fixed flow division, patient-specific pressure waveform and zero pressure. Comparisons were made for aortic flow and velocity distribution, pressure waveforms, and wall shear stress related indices.

Materials and Methods

MRI of a healthy volunteer was performed in the Robert Steiner MRI facility at Hammersmith Hospital (London, UK) on a 1.5T Philips Achieva system (Best, Netherlands). Three-dimensional (3D) bright-blood angiographic images of the thoracic aorta and proximal vessels were acquired using a navigator-gated balanced steady-state free precession sequence (voxel size $0.5 \times 0.5 \times 2$ mm). PC-MRI flow mapping planes were placed at the level of the aortic annulus and pulmonary bifurcation, normal to the aortic axis with 3D velocity encoding (VENC) gradients. VENC parameters were set 10% above the peak velocity for each velocity component. In-plane voxel size was 1.4×1.4 mm with a slice thickness of 10 mm. Retrospective cardiac gating was used and 100 time points reconstructed throughout the cardiac cycle. A central pressure measurement was performed 30 min prior to MRI using a BP Plus device (BP Plus, Uscom, Australia). This device estimates the central aortic pressure from the brachial cuff pressure: pressure wave reflection is used to reconstruct the central pressure waveform from the intra-arterial pressure oscillations according to a physics-based model (Lowe et al., 2009; Park et al., 2014). The volunteer did not have a medical history of cardiovascular diseases and gave his informed consent.

Patient-specific 3D aortic geometry, inclusive of the three supra-aortic vessels, was reconstructed from the acquired MR images using Mimics (v18, Materialise, Leuven, Belgium). Four structured meshes, consisting of 0.98 - 1.8 million hexahedral elements, were generated with ANSYS ICEM (v15.0, ANSYS Inc., Canonsburg, PA). These meshes were tested as part of a sensitivity analysis, and the chosen mesh (with ~1.5 million elements) differed from the finer mesh in the predicted maximum and minimum WSS by less than 1.5% and 1%, respectively.

The model inlet was located in the aortic root at the level of the PC-MRI flow mapping plane. PC-MR images were segmented using in-house MATLAB code and mapped to the 3D global coordinates of the model inlet by means of a coordinate transfer matrix (Cheng et al., 2016). 3D time-varying velocity profiles were derived and all three velocity components were imposed at the inlet. Fig. 1 shows the reconstructed aorta, the acquired pressure waveform and the 3D velocity profiles applied at the model inlet.

Table 1 shows the five different sets of boundary conditions specified at the model outlets, consisting of the arch branches (brachiocephalic artery, BCA; left common carotid artery, LCCA; left subclavian artery, LSA) and the aortic outlet, which is located in the descending aorta (DAo) at the level of the diaphragm. The 3-element Windkessel model (3-EWM) was included as it accounts for the influence of the vasculature distal to the model geometry. In 3-EWM the downstream vessels are represented by means of a proximal (or characteristic) resistance (R_1), a compliance (C) and a distal resistance (R_2), with a terminal (or total) resistance that can be approximated as $R_t = R_1 + R_2$ (La Disa et al., 2011). The terminal resistance was calculated as $R_t = \bar{P}/\bar{Q}$ (Les et al., 2010), where $\bar{P}$ is the mean pressure, evaluated from the acquired blood pressure waveform, and $\bar{Q}$ is the mean flow rate through each outlet. The proximal resistance was obtained as $R_1 = \rho c/A$ (Xiao et al., 2014), where c is the pulse wave speed in [m/s]. This was derived using the empirical correlation proposed by Reymond et al. (2009): $c = a_2/(2r)^{b_2}$, where $a_2 = 13.3$; $b_2 = 0.3$, and r is the vessel radius, in [mm], of the considered outlet. The distal resistance R_2 was then obtained as the difference between the terminal and the proximal resistances. The total compliance was calculated in accordance with Xiao et al. (2014) as $C = \tau/R_t$, where τ = 1.79 s is the time-constant of the exponential pressure-fall during diastole. Table 2 reports the calculated values of compliance and resistance for all the four outlets of the model.

For OBC3 and OBC4, mass flow waveforms were applied at the branches, based on a fixed flow-split which was obtained as follows: (i) The total amount of flow leaving the aorta through the three branches was calculated as the difference of the measured flow rates at the imaging planes positioned in the ascending and descending aorta; (ii) The amount of flow going into each branch was then calculated according to the relative cross-sectional areas (Zamir et al., 1992; Cheng et al., 2016). Flow rates, expressed as percentages of the inlet flow, were 11.6%, 4.7%, 3.6% and 80.1% for BCA, LCCA, LSC and DAo, respectively. The acquired patient-specific pressure waveform was reconstructed and imposed using a 20-coefficient Fourier function.

Numerical solutions were obtained using ANSYS CFX (v15.0, ANSYS, Canonsburg, PA, USA). A high-order advection scheme was adopted for spatial discretisation of the Navier–Stokes equations and a second-order implicit backward Euler scheme was chosen for temporal discretisation, with a fixed time-step of 1 ms. The maximum RMS residual was set to 10^{-5} as a convergence criterion. Flow was assumed to be laminar and blood was considered as a Newtonian fluid, with viscosity of $4 \cdot 10^{-3}$ Pa·s and a density of 1060 kg/m^3. Each simulation continued until a converged cyclic solution was reached, which required four cardiac cycles, and only the last cycle was used for further analysis. Time-averaged wall shear stress (TAWSS) and oscillatory shear index (OSI) maps were obtained using CEI Ensight (v10.1, CEI Inc., Apex, NC, USA).

Results

Comparison with PC-MRI data

The imaging plane located in the descending aorta was used for comparison purposes. Fig. 2 shows colour-coded axial velocity contours at the cross-sectional plane in the descending aorta. Three time points were selected to compare PC-MRI and computed velocity contours: T1, mid-systolic acceleration; T2, peak systole, and T3 mid-systolic deceleration. No comparison was made in diastole as the patch-wise nature of PC-MRI acquisition is amplified, due to the relatively lower velocities, making the comparison less reliable (Cheng et al, 2014).

Overall, results obtained with all OBCs show a main flow direction from superior to inferior (positive velocity values), in agreement with the PC-MR images. At mid-systolic acceleration

(T1), only OBC1 correctly captured the high velocity in the central-anterior side of the aorta. The pattern of PC-MRI velocity contours suggested the presence of secondary flow, particularly in the posterior region, and this pattern was only reproduced in the simulation results with OBC1 and, to a lesser extent, OBC2. OBC3-5 failed in this respect: OBC3 and OBC4 produced fairly uniform velocity profiles, while OBC5, despite presenting a more complex structure, did not capture the pattern seen in PC-MRI. At peak systole (T2), PC-MRI data showed a uniform velocity profile, which was well represented by all simulation results, except that with OBC5, which predicted lower velocity values. At mid-systolic deceleration (T3), a vortical structure can be noted at the left-anterior side. This feature was captured by all simulations, with OBC1-3 showing better agreement.

Quantitative comparisons of the flow rate results are shown in Fig. 3 for peak and mean flows and flow distributions among the four outlets. An overall tendency to overestimate the flow rate can be observed. While mean flow rates were very well predicted with all except OBC5, differences in peak flow rates were much larger. With regard to flow division among the outlets, OBC1-4 correctly reproduced the desired flow distribution, while OBC5 significantly underestimated the amount of flow exiting through the arch branches.

Further comparisons were made for the maximum velocity at the three selected time-points, as shown in Fig. 4. At T1 all simulations underestimated the maximum velocity value, with OBC4 presenting the best agreement (-8%) and OBC5 the worst (-52%). At T2, OBC1-4 overestimated the velocity values, while OBC5 showed an underestimation. The best agreements were found with OBC1 and 3, while OBC2 and OBC4-5 presented a similar level of absolute errors (+28%, +26%, -28%). At T3 OBC1 correctly captured the maximum velocity, showing a percentage difference lower than 0.1%. OBC2 presented the second best agreement (+3%), while OBC5 gave the worst agreement.

Pressure

Fig. 5 shows the computed aortic pressure waveforms at the inlet, together with the corresponding diastolic and systolic pressures, and the mean pressure (in brackets). OBC1-3 presented pressure values which are in agreement with the suggested pressure range for a healthy subject (Nichols, 2011), whereas OBC4 and 5 produced unrealistic values. In all cases a transient dip can be seen at about 0.3 seconds. This corresponds to the dicrotic notch, representing the closure of the aortic valve. However, only OBC1 captured a realistic pressure waveform.

Wall Shear Stress

Fig. 6 shows the TAWSS results for each case. In addition, maps of absolute differences for OBC2-5 compared to the reference case (OBC1) are also presented. OBC1-4 produced similar patterns and values of maximum TAWSS, with an absolute difference in maximum TAWSS being less than 0.1 Pa. In general, regions of relatively high TAWSS were located at the model inlet, branch roots and along the inner bend of the distal aortic arch. Although the same pattern was obtained with OBC5, it produced much higher values of TAWSS in the three branches, where a maximum value of 9.3 Pa was reached (compared to the maximum of 4.3 Pa with OBC1-4). Regions of relative low TAWSS were found in the aortic arch with all OBCs, especially in the left and posterior sides of the distal aortic arch. OBC1-4 also displayed low TAWSS at the root of the BCA in the anterior side. All cases showed lower TAWSS in the DAo than in the AAo.

Quantitative differences can be seen more clearly from the local absolute differences displayed in the lower panel in Fig. 6. The best agreement with the reference case (OBC1) was achieved with OBC3 and OBC4, presenting an absolute difference less than 0.3 Pa. OBC2 showed more notable differences in the distal aortic arch and the distal segment of DAo, but the worst agreement in TAWSS was found with OBC5, presenting large differences in the DAo and in the arch branches. Overall, all simulations produced a good agreement in the ascending aorta.

The OSI results shown in Fig. 7 revealed that the maximum value of 0.5 was present in all cases, with a wide region of high OSI (0.4-0.5) extending from the posterior side of the aortic root to the proximal right side of the aortic arch at the BCA root. High OSI was also noted at the supra-aortic branches and branch roots, and in the posterior and anterior sides of the proximal and distal DAo. OSI values were similar in the aortic arch with all OBCs, while some moderate differences (with respect to OBC1) were found in the aortic arch and the roots of arch branches. The most notable differences were observed with OBC5 where large differences occurred mainly in the arch branches and in the DAo. Comparisons of all the cases revealed that OBC5 was the worst performer with which OSI was underestimated in the descending aorta and overestimated in the aortic branches.

Discussion

Choosing appropriate boundary conditions is an important step in setting up a credible CFD model. Outlet boundary conditions are as important as inlet boundary conditions; and both can strongly influence the obtained flow patterns and hemodynamic parameters (Gallo et al. 2012; Morbiducci et al 2010; Morbiducci et al 2013). However, there is a lack of systematic study comparing the most commonly used OBCs for patient-specific modelling of blood flow in the aorta. Gallo et al. (2012) examined different boundary conditions using a realistic aortic model and highlighted the influence of outflows on the predicted results, but they did not include Windkessel-based OBC; the latter has been shown to be capable of reproducing realistic flow conditions in the carotid arteries (Morbiducci et al., 2010). In this study we compared five different sets of OBCs for CFD simulation of flow in a normal aorta reconstructed from MR images. Detailed comparisons were made of flow rate through branch vessels, peak velocity, pressure waveform, as well as WSS related indices. In addition, PC-MRI velocity maps were processed and compared with the simulation results. To eliminate the influence of inlet boundary conditions, subject-specific 3D time-varying velocity profiles were imposed at the model inlet in all simulations.

The five sets of OBCs included in this study were chosen with a decreasing amount of data necessary to set up a patient-specific simulation. For OBC1 a 3-EWM was adopted at all the model outlets, which required estimation of the model parameters (proximal and distal resistances, R_1, R_2; compliance, C), along with information about the flow through each outlet. In OBC2, 3-EWM was applied at the aortic branches, while the patient-specific pressure was applied at the aortic outlet. In OBC3 and OBC4, flow rates were imposed at the aortic branches, while the patient pressure waveform and zero-pressure were imposed at the descending aorta, respectively. These OBCs were commonly used in previous studies (e.g. Tan et al., 2012; Cheng et al., 2016). For OBC5, zero-pressure was imposed at all the model outlets, representing the simplest outlet boundary condition.

Comparisons of flow rate and flow distributions (Fig. 3) showed that Windkessel-based methods (OBC1 and OBC2) were able to maintain the expected flow split as specified in OBC3 and OBC4. However, the zero-pressure outlet condition (OBC5) failed to produce the desired flow rate and flow distribution. With OBC1-4 a good agreement was achieved between the predicted and PC-MRI measured mean flow in the DAo, although the peak flow value was overestimated with all four OBCs. This can be ascribed to several factors, most likely errors involved in the segmentation of lumen contours from PC-MR images, limited spatial resolution, noise and artefacts of the images, along with the rigid wall assumption. As for velocity data (Figs. 2 and 4), it can be argued that OBC1 and OBC2 presented the best overall agreement in velocity contours, but quantitative differences in peak velocities were large with all OBCs. With regard to pressure, while physiological pressure values were obtained with OBC1-3, only OBC1 produced a realistic shape of the pressure waveform (Fig. 5).

The analysis of TAWSS (Fig. 6) highlighted that results obtained with OBC1-4 were qualitatively similar with relatively small quantitative differences, because these four cases had similar mean flow rate and similar flow distribution among the branches. When compared with the reference case (OBC1), local differences were mainly observed in the distal aortic arch, distal DAo and in the supra-aortic branches, with OBC2 displaying more notable differences than OBC3 and OBC4. The fact that results obtained with OBC3 and OBC4 were almost identical suggested that TAWSS and OSI in the aorta were not sensitive to the exact pressure value specified at the DAo outlet. However, OBC5 showed distinctively different results, with a peak TAWSS more than doubled (+116%) compared to the other cases. This was due to the dramatically different flow distribution among the branches as a result of the zero-pressure BC at all outlets. Not surprisingly, OBC5 also had a distinctly different OSI pattern. While absolute differences in OSI did not appear to be significant with OBC2-4, notable differences could be seen in areas where TAWSS was low, suggesting that low shear regions (i.e. potential atheroprone regions) would be subject to larger uncertainty for the evaluation of OSI. One such area was located at the level of the supra-aortic branches, which is known to be prone to vascular pathologies (Mohamied et al., 2015); it is therefore important to be aware of the non-negligible influences of OBCs on the evaluated WSS and OSI in these regions.

Limited data availability is a common issue for patient-specific simulations of flow in the aorta. It is, therefore, important to be able to optimise the use of available clinical data and to assess the level of agreement that can be achieved with *in vivo* measurements. In this paper, we have shown how simulation results can be influenced by different combinations of OBCs based on commonly available clinical data. This comparative study can serve as a useful reference for future choices of OBCs. Overall, simulation results obtained with OBC1 showed the best agreement with *in vivo* data, along with the most physiological pressure waveforms and values. A good agreement was also obtained with OBC3, but no apparent advantage was noticed with OBC2 which combined 3-EWM with patient-specific pressure waveform. While our results suggest that Windkessel OBCs should be preferred for patient-specific simulations of aortic flow, it must be noted that more complex lumped parameter boundary conditions also exist and have been used for closed-loop modelling (Kim et al., 2010; Kung et al., 2013; Baretta et al., 2011; Pant et al., 2014). Closed-loop models have the advantage of accounting for the entire circulatory system, including the heart and the pulmonary circulation, but they require even more patient data for estimation of model parameters or more sophisticated tuning method (Pant et al., 2014). In addition, closed-loop models do not allow for the imposition of patient-specific time-varying velocity profile at model inlet. On balance, we believe that the combination of Windkessel OBCs and image-based 3D CFD models provides a practical and physiologically valid solution to quantitative analysis of blood flow in patient-specific settings. Moreover, Windkessel type OBCs can be very useful for predictive modelling aimed at evaluating the hemodynamic performance of surgical or interventional procedures when post-operative pressure or flow are unknown (Baretta et al., 2011; Kung et al., 2013; Pant et al., 2014).

The CFD model employed in this study involved several assumptions which should be noted. First, the aortic wall was assumed as rigid. As a result, quantitative comparisons between the predicted and PC-MR measured velocities were limited by the fact that the aortic lumen expands and contracts during a cardiac cycle, whereas the CFD model assumed a fixed lumen area. Second, the flow split between the aortic branches was based on the cross-sectional area of each branch. This is not entirely true as flow leaving the arch branches would also depend on the oxygen demand of the downstream tissues, which is patient-specific and should be obtained by PC-MRI in future studies. Finally, the acquired pressure waveform was obtained non-invasively, and despite being representative of the subject's central pressure, uncertainties might have been introduced when synchronising the pressure with MRI-based flow waveform. In addition, pressure differences between the model inlet and outlets were assumed to be negligible.

Conclusions

This study confirmed that the choice of outlet boundary conditions can have a profound impact on the evaluation of aortic hemodynamics. Overall, our results show that even with a limited amount of patient-specific data, a good agreement can be achieved with *in vivo* hemodynamics by using Windkessel-based OBCs. Furthermore, it has been shown that Windkessel-based outlet boundary conditions (3-EWM) can also reproduce physiological aortic pressure waveforms, and should be used as the preferred outlet boundary condition for open-loop modelling of aortic flow with multiple outlets.

Conflict of Interest Statement

All authors have no personal nor financial relationships with organisation or people that could have biased the present work.

Acknowledgements

This work was supported by the European Commission within the Horizon 2020 Framework through the MSCA-ITN-ETN European Training Networks (project number 642458). MR images were acquired as part of a project supported by the National Institute for Health Research (NIHR) Biomedical Research Centre (based at Imperial College Healthcare NHS Trust and Imperial College London), and the NIHR Cardiovascular Biomedical Research Unit (based at the Royal Brompton and Harefield NHS Foundation Trust). D.P.O'R. is funded by the MRC.

References

AUGST, A. D., BARRATT, D. C., HUGHES, A. D., THOM, S. A. & XU, X. Y. 2003. Various issues relating to computational fluid dynamics simulations of carotid bifurcation flow based on models reconstructed from three-dimensional ultrasound images. Proceedings of the Institution of Mechanical Engineers, Part H: *Journal of Engineering in Medicine*, 217, 393–403.

BARETTA, A., CORSINI, C., YANG, W., VIGNON-CLEMENTEL, I. E., MARSDEN, A. L., FEINSTEIN, J. A., HSIA, T.-Y., DUBINI, G., MIGLIAVACCA, F., PENNATI, G. 2011. Virtual surgeries in patients with congenital heart disease: a multi-scale modelling test case. Philosophical Transactions of the Royal Society of London A: *Mathematical, Physical and Engineering Sciences*, 369, 4316-4330.

CAMPBELL, I.C., RIES, J., DHAWAN, S.S., QUYYUMI, A.A., TAYLOR, W. & OSHINSKI, J.N. 2012. Effect of Inlet Velocity Profiles on Patient-Specific Computational Fluid Dynamics Simulations of the Carotid Bifurcation. *Journal of Biomechanical Engineering*, 134, 051001.

CHENG, Z., JULI, C., WOOD, N.B., GIBBS, R.G.J. & XU, X.Y. 2014. Predicting flow in aortic dissection: Comparison of computational model with PC-MRI velocity measurements. *Medical Engineering & Physics*, 36, 1176-1184.

CHENG, Z., KIDHER, E., JARRAL, O. A., O'REGAN, D. P., WOOD, N. B., ATHANASIOU, T. & XU, X. Y. 2016. Assessment of hemodynamic conditions in the aorta following root replacement with composite valve-conduit graft. *Annals of Biomedical Engineering*, 44, 1392-1404.

GALLO, D., DE SANTIS, G., NEGRI, F., TRESOLDI, D., PONZINI, R., MASSAI, D., DERIU, M. A., SEGERS, P., VERHEGGHE, B., RIZZO, G. & MORBIDUCCI, U. 2012. On the use of in vivo measured flow rates as boundary conditions for image-based hemodynamic models of the human aorta: implications for indicators of abnormal flow. *Annals of Biomedical Engineering*, 40, 729-741.

KIM, H. J., VIGNON-CLEMENTEL, I. E., COOGAN, J. S., FIGUEROA, C. A., JANSEN, K. E., & TAYLOR, C. A. 2010. Patient-specific modeling of blood flow and pressure in human coronary arteries. *Annals of Biomedical Engineering*, 38, 3195-3209.

KUNG, E., BARETTA, A., BAKER, C., ARBIA, G., BIGLINO, G., CORSINI, C., SCHIEVANO S., VIGNON-CLEMENTEL I.E., DUBINI G., PENNATI G., TAYLOR, A., DORFMAN, A., HLAVACEK, A.M., MARSDEN, A.L., HSIA, T.-Y., MIGLIAVACCA, F. 2013. Predictive modeling of the virtual Hemi-Fontan operation for second stage single ventricle palliation: two patient-specific cases. *Journal of Biomechanics*, 46, 423-429.

LADISA, J. F., FIGUEROA, C. A., VIGNON-CLEMENTEL, I. E., KIM, H. J., XIAO, N., ELLWEIN, L. M., CHAN, F.P., FEINSTEIN, J.A. & TAYLOR, C. A. 2011. Computational simulations for aortic coarctation: representative results from a sampling of patients. *Journal of Biomechanical Engineering*, 133, 091008.

LES, A. S., SHADDEN, S. C., FIGUEROA, C. A., PARK, J. M., TEDESCO, M. M., HERFKENS, R. J., DALMAN, R.L & TAYLOR, C. A. 2010. Quantification of hemodynamics in abdominal aortic aneurysms during rest and exercise using magnetic resonance imaging and computational fluid dynamics. *Annals of Biomedical Engineering*, 38, 1288-1313.

LOWE A, HARRISON, W., EL-AKLOUK, E., RUYGROK, P., AL-JUMAILY, A.M. 2009. Non-invasive model-based estimation of aortic pulse pressure using suprasystolic brachial pressure waveforms. *Journal of Biomechanics*, 42:2111–2115,

MOHAMIED, Y., ROWLAND, E. M., BAILEY, E. L., SHERWIN, S. J., SCHWARTZ, M. A., & WEINBERG, P. D. 2015. Change of Direction in the Biomechanics of Atherosclerosis. *Annals of Biomedical Engineering*, 43, 16-25.

MORBIDUCCI, U., GALLO, D., MASSAI, D., CONSOLO, F., PONZINI, R., ANTIGA, L., BIGNARDI, C., DERIU, M.A. & REDAELLI, A. 2010. Outflow conditions for image-based hemodynamic models of the carotid bifurcation: implications for indicators of abnormal flow. *Journal of Biomechanical Engineering*, 132, 091005.

MORBIDUCCI, U., PONZINI, R., GALLO, D., BIGNARDI, C. & RIZZO, G. 2013. Inflow boundary conditions for image-based computational hemodynamics: impact of idealized versus measured velocity profiles in the human aorta. *Journal of Biomechanics*, 46, 102-109.

NICHOLS, W., O'ROURKE, M., & VLACHOPOULOS, C. 2011 (Eds.). McDonald's blood flow in arteries: theoretical, experimental and clinical principles. CRC Press.

PANT, S., FABRÈGES, B., GERBEAU, J. F., & VIGNON-CLEMENTEL, I. E. 2014. A methodological paradigm for patient-specific multiscale CFD simulations: from clinical measurements to parameter estimates for individual analysis. *International Journal for Numerical Methods in Biomedical Engineering*, 30, 1614-1648.

PARK, C.M.; KOROLKOVA, O., DAVIES, J.E.; PARKER, K.H.; SIGGERS, J.H.; MARCH, K.; TILLIN, T.; CHATURVEDI, N.; HUGHES, A.D. 2014. Arterial pressure: agreement between a brachial cuff-based device and radial tonometry. *Journal of Hypertension*, 32, 865–872

REYMOND, P., MERENDA, F., PERREN, F., RÜFENACHT, D. & STERGIOPULOS, N. 2009. Validation of a one-dimensional model of the systemic arterial tree. *American Journal of Physiology-Heart and Circulatory Physiology*, 297, H208-H222.

TAN, F. P. P., XU, X. Y., TORII, R., WOOD, N. B., DELAHUNTY, N., MULLEN, M., MOAT, N. & MOHIADDIN, R. 2012. Comparison of aortic flow patterns before and after transcatheter aortic valve implantation. *Cardiovascular Engineering and Technology*, 3, 123-135.

VAN DER GIESSEN, A. G., GROEN, H. C., DORIOT, P. A., DE FEYTER, P. J., VAN DER STEEN, A. F., VAN DE VOSSE, F. N., WENTZEL, J.J. & GIJSEN, F. J. 2011. The influence of boundary conditions on wall shear stress distribution in patients specific coronary trees. *Journal of Biomechanics*, 44, 1089-1095.

VIGNON-CLEMENTEL, I. E., FIGUEROA, C. A., JANSEN, K. E. & TAYLOR, C. A. 2006. Outflow boundary conditions for three-dimensional finite element modeling of blood flow and pressure in arteries. *Computer Methods in Applied Mechanics and Engineering*, 195, 3776-3796.

XIAO, N., ALASTRUEY, J. & ALBERTO FIGUEROA, C. 2014. A systematic comparison between 1-d and 3-d hemodynamics in compliant arterial models. *International Journal for Numerical Methods in Biomedical Engineering*, 30, 204-231.

ZAMIR, M., SINCLAIR, P., & WONNACOTT, T. H. 1992. Relation between diameter and flow in major branches of the arch of the aorta. *Journal of Biomechanics*, 25, 1303–1310.

Figure 1: 3D reconstruction of the aorta, together with the PC-MRI flow mapping planes. Acquired central pressure waveform and snapshots of 3D velocity profiles applied at the model inlet. The corresponding time points are defined along a flow waveform shown at the bottom right corner.

Figure 2: Comparison of the axial velocity contours at a location in the descending aorta where PC-MR flow mapping was acquired. Comparisons are made at mid-systolic acceleration (T1, top row), peak systole (T2, middle row), and mid-systolic deceleration (T3, bottom row). Positive values indicate flow in the head-foot direction. Secondary velocity vectors are superimposed on the velocity contours to show vortical motion.

Figure 3: Top: Comparison of mean (bars) and peak (stars) flow rates at a location in the descending aorta between PC-MRI measurements and simulation results obtained with the five sets of OBCs. Bottom: Mean flow distribution among the four outlets, expressed as a percentage of the inlet flow. DAo: descending aorta, BCA: brachiocephalic artery, LCCA: left common carotid artery, LSCA: left subclavian artery.

Figure 4: Maximum velocity values derived from PC-MRI data and from simulation results obtained with the five sets of OBCs at three different time-points. T1, T2 and T3 are defined in Fig. 1. Percentage differences with respect to the PC-MRI data are reported, with red colour highlighting the best result for each time-point.

Figure 5: Computed aortic pressure waveforms. For each case diastolic, systolic and mean (in brackets) pressures are reported at the top right corner.

Figure 6: Top: Time-averaged wall shear stress (TAWSS) results obtained with the five sets of OBCs. Bottom: local absolute differences in TAWSS as compared to results obtained with OBC1.

Figure 7: Top: Oscillatory shear index (OSI) results obtained with the five sets of OBCs. Bottom: local absolute differences in OSI as compared to results obtained with OBC1.

Table 1: Different sets of boundary conditions specified at the model inlet and outlets. The model outlets are located at the arch branches (AoB) and in the descending aorta (DAo), at the level of the diaphragm.

Case Name	Inlet BC	AoB BC	DAo BC
OBC1	3D patient-specific velocity profiles	3-EWM	3-EWM
OBC2	3D patient-specific velocity profiles	3-EWM	Patient-specific pressure waveform
OBC3	3D patient-specific velocity profiles	Mass flow waveforms	Patient-specific pressure waveform
OBC4	3D patient-specific velocity profiles	Mass flow waveforms	0-pressure
OBC5	3D patient-specific velocity profiles	0-pressure	0-pressure

Table 2: Values for parameters used in the 3-EWM. R_1=proximal resistance, R_2= distal resistance, C= vessel compliance. BCA= brachiocephalic artery, LCCA=left common carotid artery, LSA= left subclavian artery, DAo= descending aorta.

	R_1 [10^7 Pa·s·m^{-3}]	R_2 [10^8 Pa·s·m^{-3}]	C [10^{-10} m^3·Pa^{-1}]
BCA	6.3	17.1	10.1
LCCA	17.6	41.7	4.1
LSA	24.1	54.7	3.1
DAo	1.7	2.4	69.7

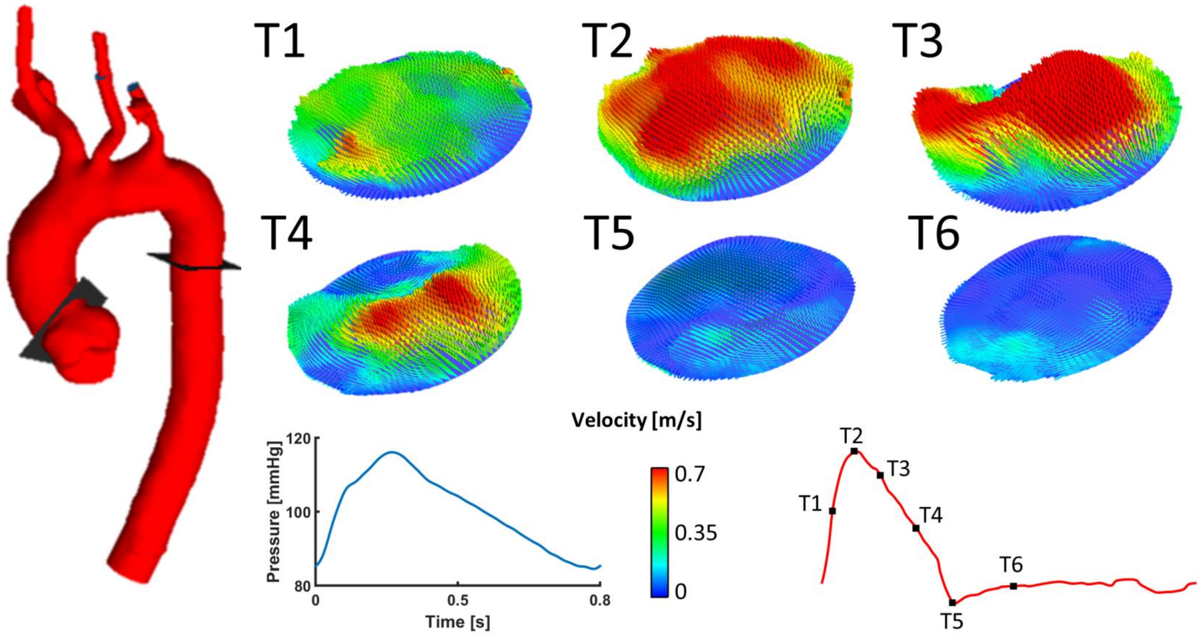

Figure 1

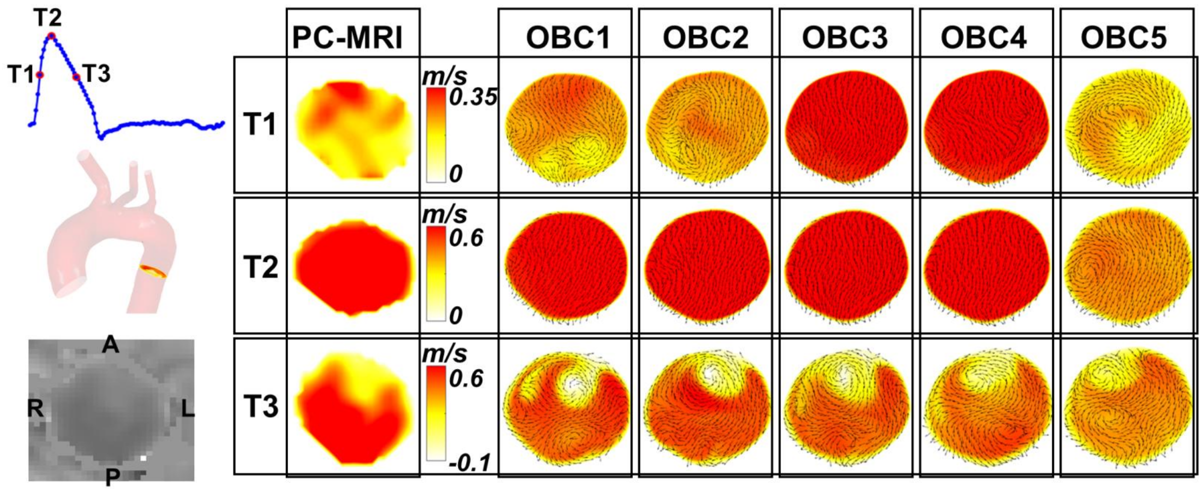

Figure 2

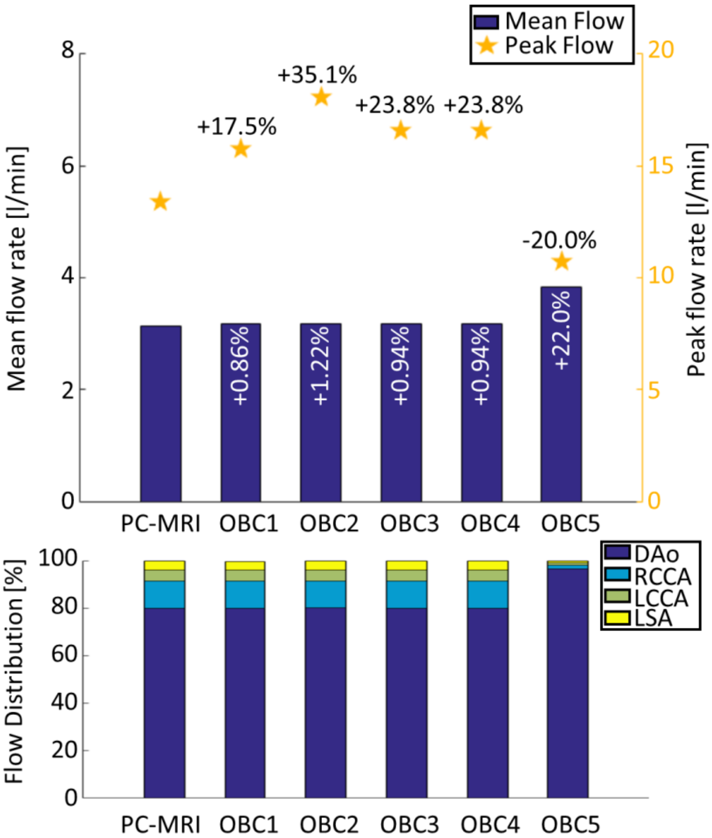

Figure 3

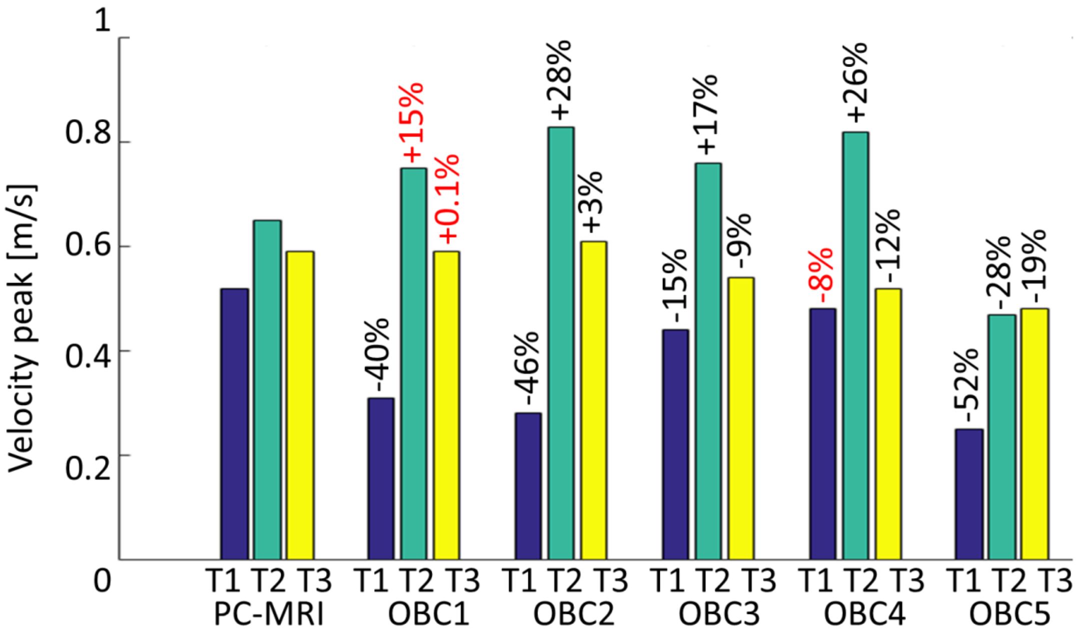

Figure 4

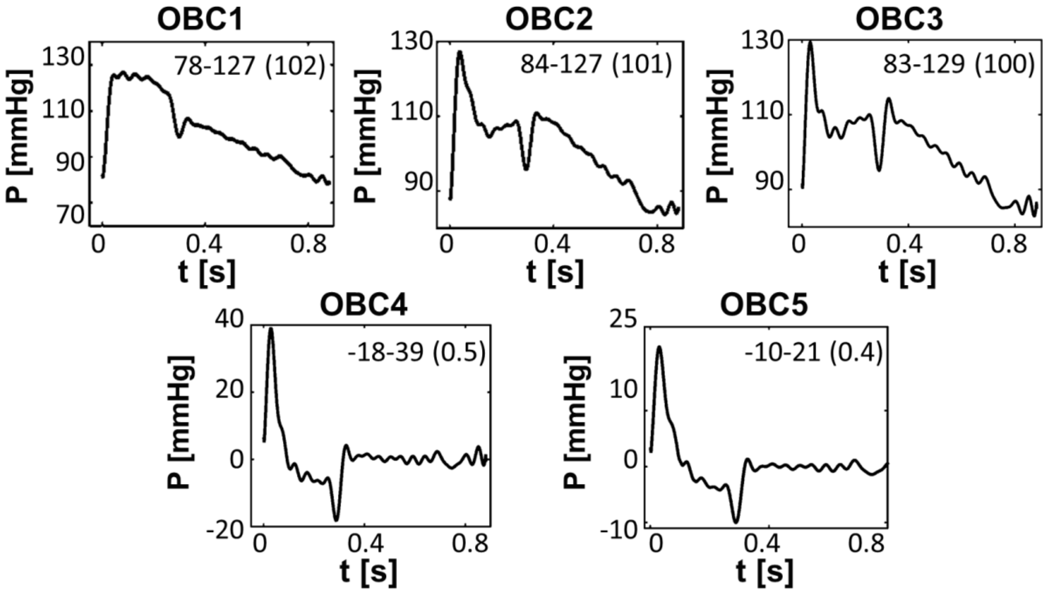

Figure 5

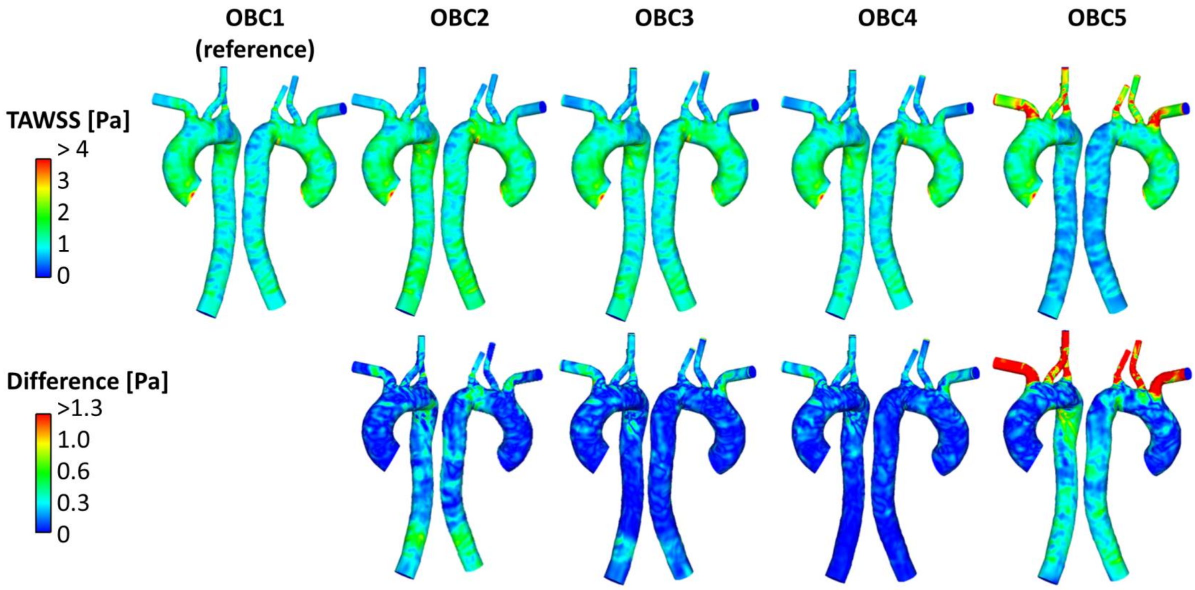

Figure 6

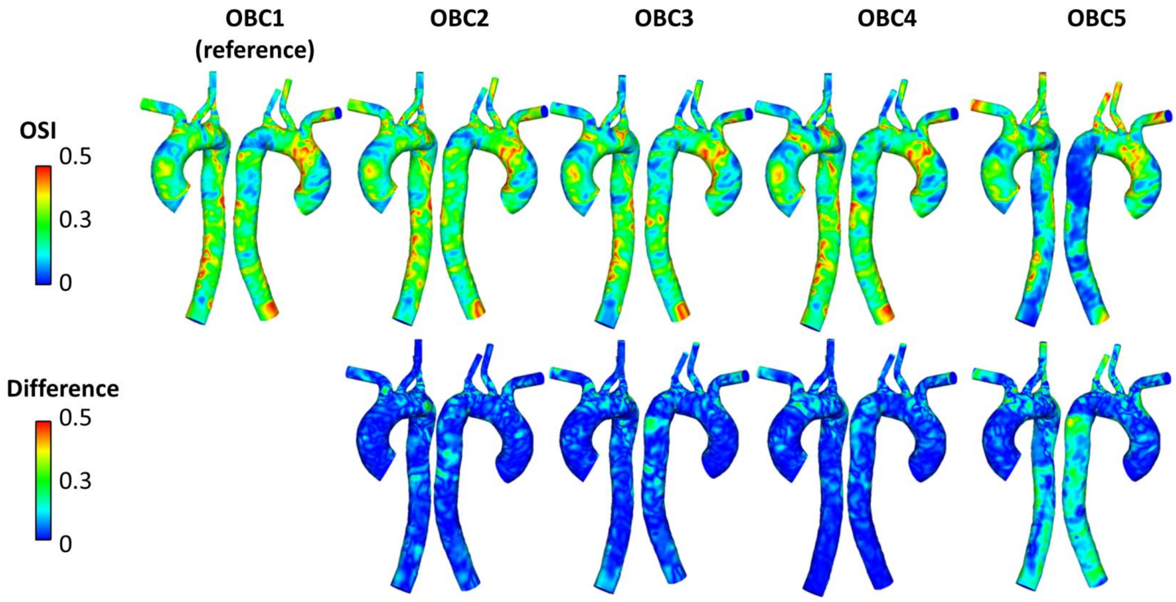
OBC1
(reference)
OBC2
OBC3
OBC4
OBC5
OSI
0.5
0.3
0
Difference
0.5
0.3
0

Figure 7